REPORT DOCUMENTATION PAGE

Form Approved OMB NO. 0704-0188

1. REPORT DATE (DD-MM-YYYY)	2. REPORT TYPE	3. DATES COVERED (From - To)
12-12-2013	Final Report	15-Jul-2009 - 14-Jul-2013

4. TITLE AND SUBTITLE
Final Report W911NF-09-1-0147: High performance nuclear magnetic resonance imaging using magnetic resonance force microscopy

5a. CONTRACT NUMBER
W911NF-09-1-0147

5b. GRANT NUMBER

5c. PROGRAM ELEMENT NUMBER
611102

6. AUTHORS
P. Chris Hammel

5d. PROJECT NUMBER

5e. TASK NUMBER

5f. WORK UNIT NUMBER

7. PERFORMING ORGANIZATION NAMES AND ADDRESSES
Ohio State University Research Foundation
Office of Sponsored Programs
1960 Kenny Rd.
Columbus, OH 43210 -1063

8. PERFORMING ORGANIZATION REPORT NUMBER

9. SPONSORING/MONITORING AGENCY NAME(S) AND ADDRESS (ES)
U.S. Army Research Office
P.O. Box 12211
Research Triangle Park, NC 27709-2211

10. SPONSOR/MONITOR'S ACRONYM(S)
ARO

11. SPONSOR/MONITOR'S REPORT NUMBER(S)
56030-MS.5

12. DISTRIBUTION AVAILIBILITY STATEMENT
Approved for Public Release; Distribution Unlimited

13. SUPPLEMENTARY NOTES
The views, opinions and/or findings contained in this report are those of the author(s) and should not contrued as an official Department of the Army position, policy or decision, unless so designated by other documentation.

14. ABSTRACT
We summarize the key advances resulting from our research program supported by ARO award W911NF-09-1-0147 between July 15, 2009 and July 14, 2013. We have used ultra-sensitive Magnetic Resonance Force Microscopy detection Electron Spin Resonance, using (ESR-MRFM), to perform spatially resolved scanned probe studies of spin dynamics in nanoscale ensembles of few electron spins of varying size. Our research culminated in observation that the distinction between two channels of energy flow from and within a spin system, typically characterized the spin-lattice relaxation time T_1 and the spin-spin relaxation time T_2 that are rigorously distinct

15. SUBJECT TERMS
ESR, MRFM, NMR, Spin Transport

16. SECURITY CLASSIFICATION OF:			17. LIMITATION OF ABSTRACT	15. NUMBER OF PAGES	19a. NAME OF RESPONSIBLE PERSON
a. REPORT	b. ABSTRACT	c. THIS PAGE			Peter Hammel
UU	UU	UU	UU		19b. TELEPHONE NUMBER 614-247-6928

Report Title

Final Report W911NF-09-1-0147: High performance nuclear magnetic resonance imaging using magnetic resonance force microscopy

ABSTRACT

We summarize the key advances resulting from our research program supported by ARO award W911NF-09-1-0147 between July 15, 2009 and July 14, 2013. We have used ultra-sensitive Magnetic Resonance Force Microscopy detection Electron Spin Resonance, using (ESR-MRFM), to perform spatially resolved scanned probe studies of spin dynamics in nanoscale ensembles of few electron spins of varying size. Our research culminated in observation that the distinction between two channels of energy flow from and within a spin system, typically characterized the spin-lattice relaxation time T_1 and the spin-spin relaxation time T_2 that are rigorously distinct in macroscopic systems become indistinguishable in nanoscale systems. This is because spin transport mediated by mutual spin flip-flop diffusion---arising from a T_2-like process---in a nanoscale quasi-1D spin nanowire can transfer energy from the measured spin system to the thermal reservoir outside the measured volume---behavior typical of T_1 processes. The spin nanowire we created in diamond by means of patterned nitrogen ion implantation represents an intriguing prototype element of a spintronic device in an attractive and widely used wide band gap semiconductor. ESR-MRFM, a scanned probe method capable of spatially resolved magnetic resonance detection, offers a powerful approach to understanding the spin properties and dynamics in the device-like environments where their dynamics and lifetime will be influenced by nanoscale confinement. Our theoretical model that explains the observed spin dynamics in confined nanoscale spin structures are supported by extensive numerical modeling that agree well with our experimental data. Using our understanding of the electron spin dynamics in confined nanoscale structures, we developed an improved measurement protocol, pi-OSCAR, that we that we used to demonstrate spectroscopic measurements on nanoscale spin ensembles of few electron spins. Our demonstration of nanoscale, spatially resolved measurements of spin dynamics in quasi 1D spin nanowires in diamond, presented in a manuscript entitled ``The effect of spin transport on lifetime in nanoscale systems," is currently under review at Nature Nanotechnology.

Enter List of papers submitted or published that acknowledge ARO support from the start of the project to the date of this printing. List the papers, including journal references, in the following categories:

(a) Papers published in peer-reviewed journals (N/A for none)

Received		Paper
02/13/2013	3.00	K. C. Fong, M. R. Herman, P. Banerjee, D. V. Pelekhov, P. C. Hammel. Spin lifetime in small ensembles of electron spins measured by magnetic resonance force microscopy, Physical Review B, (12 2011): 220405. doi: 10.1103/PhysRevB.84.220405
12/12/2013	4.00	Jeremy Cardellino, Nicolas Scozzaro, Michael Herman, Andrew J. Berger, Chi Zhang, Kin Chung Fong, Ciriyam Jayaprakash, Denis V. Pelekhov, P. Chris Hammel. The effect of spin transport on lifetime in nanoscale systems, Nature Nanotechnology (submitted), (11 2013): 0. doi:
TOTAL:	**2**	

Number of Papers published in peer-reviewed journals:

(b) Papers published in non-peer-reviewed journals (N/A for none)

Received Paper

TOTAL:

Number of Papers published in non peer-reviewed journals:

(c) Presentations

"Spin Transport Driven by Magnetization Dynamics: Nanoscale studies of spin dynamics," invited talk presented at the 8th ASRC International Workshop on Spin Mechanics, Tokai,Japan, 24–26 February 2013,

"Nanoscale scanning probe ferromagnetic resonance imaging using localized modes," presented at the March Meeting of the American Physical Society, Dallas TX, March 2011

"Nanoscale scanned probe ferromagnetic resonance imaging using localized modes," presented at the 3rd nano-MRI research conference: Exploring the Frontiers of Magnetic Resonance Imaging to be held at Le Tremblay sur Mauldre, France, 12–16 July 2010

"Scanned probe imaging of spin physics," presented at the International Workshop on Novel Magnetic Materials, Leibniz Institute for Solid State and Materials Research, 23–25 August 2010, Dresden, Germany

"Spin Transport Driven by Magnetization Dynamics," Colloquium presented at Boston College Department of Physics, Chestnut Hill, MA, December 5, 2012

Number of Presentations: 5.00

Non Peer-Reviewed Conference Proceeding publications (other than abstracts):

Received Paper

TOTAL:

Number of Non Peer-Reviewed Conference Proceeding publications (other than abstracts):

Peer-Reviewed Conference Proceeding publications (other than abstracts):

Received	Paper

TOTAL:

Number of Peer-Reviewed Conference Proceeding publications (other than abstracts):

(d) Manuscripts

Received		Paper
09/04/2011	1.00	K.C. Fong, M. R. Herman,, P. Banerjee, D. V. Pelekhov, P. C. Hammel. Spin Lifetime in Small Electron Spin Ensembles Measured by Magnetic ResonanceForce Microscopy, Physical Review B (07 2011)

TOTAL: **1**

Number of Manuscripts:

Books

Received	Paper

TOTAL:

Patents Submitted

Patents Awarded

Awards

Graduate Students

NAME	PERCENT_SUPPORTED	Discipline
Michael Herman	0.53	
Jeremy Cardellino	0.49	
Nicolas Scozzaro	0.14	
Carola Purser	0.03	
FTE Equivalent:	**1.19**	
Total Number:	**4**	

Names of Post Doctorates

NAME	PERCENT_SUPPORTED
FTE Equivalent:	
Total Number:	

Names of Faculty Supported

NAME	PERCENT_SUPPORTED	National Academy Member
P. Chris Hammel	0.07	
FTE Equivalent:	**0.07**	
Total Number:	**1**	

Names of Under Graduate students supported

NAME	PERCENT_SUPPORTED	Discipline
Ian Brandeberry	0.04	Physics
FTE Equivalent:	**0.04**	
Total Number:	**1**	

Student Metrics

This section only applies to graduating undergraduates supported by this agreement in this reporting period

The number of undergraduates funded by this agreement who graduated during this period: 1.00

The number of undergraduates funded by this agreement who graduated during this period with a degree in science, mathematics, engineering, or technology fields:..... 1.00

The number of undergraduates funded by your agreement who graduated during this period and will continue to pursue a graduate or Ph.D. degree in science, mathematics, engineering, or technology fields:..... 0.00

Number of graduating undergraduates who achieved a 3.5 GPA to 4.0 (4.0 max scale):..... 0.00

Number of graduating undergraduates funded by a DoD funded Center of Excellence grant for Education, Research and Engineering:..... 0.00

The number of undergraduates funded by your agreement who graduated during this period and intend to work for the Department of Defense 0.00

The number of undergraduates funded by your agreement who graduated during this period and will receive scholarships or fellowships for further studies in science, mathematics, engineering or technology fields: 0.00

Names of Personnel receiving masters degrees

NAME
Total Number:

Names of personnel receiving PHDs

NAME	
Michael Herman	
Total Number:	**1**

Names of other research staff

NAME	PERCENT_SUPPORTED
Iouri V. Oboukhov	0.16
Denis V. Pelekhov	0.09
FTE Equivalent:	**0.25**
Total Number:	**2**

Sub Contractors (DD882)

Inventions (DD882)

Scientific Progress

See Attachment

Technology Transfer

Final Report W911NF-09-1-0147: High performance nuclear magnetic resonance imaging using magnetic resonance force microscopy

P. Chris Hammel
Department of Physics, The Ohio State University

We summarize the key advances resulting from our research program supported by ARO award W911NF-09-1-0147 between July 15, 2009 and July 14, 2013. We have used ultra-sensitive Magnetic Resonance Force Microscopy detection Electron Spin Resonance, using (ESR-MRFM), to perform spatially resolved scanned probe studies of spin dynamics in nanoscale ensembles of few electron spins of varying size. Our research culminated in observation that the distinction between two channels of energy flow from and within a spin system, typically characterized the spin-lattice relaxation time T_1 and the spin-spin relaxation time T_2 that are rigorously distinct in macroscopic systems become indistinguishable in nanoscale systems. This is because spin transport mediated by mutual spin flip-flop diffusion—arising from a T_2-like process—in a nanoscale quasi-1D spin nanowire can transfer energy from the measured spin system to the thermal reservoir outside the measured volume—behavior typical of T_1 processes. The spin nanowire we created in diamond by means of patterned nitrogen ion implantation represents an intriguing prototype element of a spintronic device in an attractive and widely used wide band gap semiconductor. ESR-MRFM, a scanned probe method capable of spatially resolved magnetic resonance detection, offers a powerful approach to understanding the spin properties and dynamics in the device-like environments where their dynamics and lifetime will be influenced by nanoscale confinement. Our theoretical model that explains the observed spin dynamics in confined nanoscale spin structures are supported by extensive numerical modeling that agree well with our experimental data. Using our understanding of the electron spin dynamics in confined nanoscale structures, we developed an improved measurement protocol, pi-OSCAR, that we that we used to demonstrate spectroscopic measurements on nanoscale spin ensembles of few electron spins. Our demonstration of nanoscale, spatially resolved measurements of spin dynamics in quasi 1D spin nanowires in diamond, presented in a manuscript entitled "The effect of spin transport on lifetime in nanoscale systems," is currently under review at *Nature Nanotechnology*. This advance involved several advances:

- Creation of an integrated model of spin dynamics and spin transfer across interface in nanoscale spin ensembles in the presence of large magnetic field gradients.
- Microscopic Monte Carlo simulation of spin-flip mediated spin transport in quasi 1D systems.
- Development of a data deconvolution protocol enabling spectroscopic studies of nanoscale spin ensembles.
- Development and detailed analysis of a new ESR-MRFM detection protocol—pi-OSCAR—that improves control over the size of the measured spin ensemble.

These achievements were enabled by improvements in ESR-MRFM technique and detection. These included improvement of the signal-to-noise ratio of the measurement apparatus, preliminary studies of the material systems for the current and next-step experiments with the ESR-MRFM, and fabrication of the nitrogen implanted spin nanowires; these include:

- Detection of ~ 13 electron spins with high signal-to-noise ratio through improved MRFM cantilever visibility, quality factor and microwave delivery.
- Custom N-implanted diamond samples including uniformly doped samples and quasi 1D spin nanowires were fabricated for ESR-MRFM imaging.
- P1 and NV centers in nitrogen implanted diamond samples were simultaneously measured demonstrating the ability to detect and characterize defect.
- Conventional EPR and ENDOR characterization of P1 centers in diamond for nuclear spin detection through electron spin detection.
- Studies of interfacial magnetism in $LaAlO_3/SrTiO_3$(LAO/STO).

I. INTRODUCTION

We summarize the key advances resulting from our research program supported by ARO award W911NF-09-1-0147 between July 15, 2009 and July 14, 2013. We have used ultra-sensitive Magnetic Resonance Force Microscopy detection Electron Spin Resonance, using (ESR-MRFM), to perform spatially resolved scanned probe studies of spin dynamics in nanoscale ensembles of few electron spins of varying size. Our research culminated in observation that the distinction between two channels of energy flow from and within a spin system, typically characterized the spin-lattice relaxation time T_1 and the spin-spin relaxation time T_2 that are rigorously distinct in macroscopic systems become indistinguishable in nanoscale systems. This is because spin transport mediated by mutual spin flip-flop diffusion—arising from a T_2-like process—in a nanoscale quasi-1D spin nanowire can transfer energy from the measured spin system to the thermal reservoir outside the measured volume—behavior typical of T_1 processes. The spin nanowire we created in diamond by means of patterned nitrogen ion implantation represents an intriguing prototype element of a spintronic device in an attractive and widely used wide band gap semiconductor. ESR-MRFM, a scanned probe method capable of spatially resolved magnetic resonance detection, offers a powerful approach to understanding the spin properties and dynamics in the device-like environments where their dynamics and lifetime will be influenced by nanoscale confinement. Our theoretical model that explains the observed spin dynamics in confined nanoscale spin structuresare supported by extensive numerical modeling that agree well with our experimental data. Using our understanding of the electron spin dynamics in confined nanoscale structures, we developed an improved measurement protocol, pi-OSCAR, that we that we used to demonstrate spectroscopic measurements on nanoscale spin ensembles of few electron spins. The results of our studies will be presented in a manuscript, "The effect of spin transport on lifetime in nanoscale systems," currently under review at *Nature Nanotechnology*.

These achievements were supported, particularly in the earlier stages of the project, by improvements of the ESR-MRFM technique. These included improvement of the signal-to-noise ratio of the measurement apparatus, preliminary studies of the material systems for the current and next-step experiments with the ESR-MRFM, and fabrication of the nitrogen implanted spin nanowires.

These studies have advanced ability to study spin properties of nanoscale structures and have explored new approaches to spintronics in diamond, a wide bandgap semiconductors that could be attractive for scientific and technological problems of importance to the DoD, industry, and society. This research is based on our unique capability for ultrasensitive mechanical detection of magnetic resonance. This research has benefited from a close interaction with our collaborators including Dr. D. Rugar at IBM (Almaden, CA), Prof. R. Budakian at UIUC (Urbana-Champaign, IL) and Prof. C. H. Ahn at Yale University (New Haven, CT).

The most interesting result of our studies is the ESR-MRFM study of spin dynamics quasi 1D spin nanowires in diamond. The measurements show that the dynamics of the electron spins in a nanoscale ensemble are dominated by transfer of the spin moment across the spatial boundaries of the measurement volume via spin diffusion facilitated by mutual spin flip transitions. Also interesting is the fact that these measurements were conducted by coupling spin magnetic moments to the high gradient magnetic field of the ESR-MRFM probe which will suppress the mutual spin flip diffusion. Our investigation of this seeming contradiction led us to consider several explanations for the observed effect: these included the possibility that the strongly anisotropic hyperfine interaction of an electron on P1 center with the associated ^{14}N atom could be responsible for overcoming this suppression. To resolve this question, we conducted an extensive numerical microscopic Monte Carlo simulation of the spin diffusion assisted spin transport in quasi 1D systems (see Sec. III) and developed a method for ESR-MRFM data deconvolution enabling spectroscopic measurements on nanoscale spin ensem-

bles (see Sec. IV). Our investigations show that the observed absence of spin diffusion suppression stems from the inhomogeneous ESR line broadening of an electron on P1 center due to the distortions introduced by ion implantation. These findings are summarized in Sec. II. We have also conducted a detailed analysis of a new ESR-MRFM spin manipulation protocol that allows improved control over the measurement volume in ESR-MRFM experiment (see Sec. V).

II. SPIN DYNAMICS IN NANOSCALE SPIN ENSEMBLES

Spin centers in diamond—such as nitrogen vacancy (NV) centers, nitrogen (P1) centers, or the newly discovered ST1 center [1]—are of great interest for spintronics and quantum computation and have proven to be valuable platforms for studying the role of spin interactions [2]. Spins which are well-isolated from their environment exhibit long coherence times [3–5], yet spin interactions are necessary for entanglement, transport, and read-out schemes [6]. Here, we directly observe spin transport in dipole-coupled P1 spins in thermal equilibrium. Since diamond is an insulator, charge motion is completely absent from this spin transport. The transport is confined to a nano-scale quasi-1D 'spin wire' where the spin density leads to appreciable dipolar coupling and spin flip-flop interactions. In samples with long T_1 — such as our own — this type of spin transport could result in highly efficient, even reversible [7], pure spin currents. Furthermore, by implementing a magnetic resonance protocol that improves spatial resolution, we demonstrate selective detection of different nuclear spin states and measure the hyperfine spectrum within the spin wire. Our measurements probe intrinsic spin dynamics at the nanometer scale, providing critical information for practical devices which seek to control spin.

Spintronics research has largely focused on two regimes — spin transport by conduction electrons, modeled as a continuum spin density [8], and the isolated single spin "qubit" [9, 10]. Appropriate coupling between spins could allow for efficient spin transport, while preserving long spin lifetimes. For example, a spin flip-flop — the simultaneous flipping of a pair of anti-aligned neighboring spins due to their dipolar interaction — conserves magnetization. Hence, successive flip-flops can result in a pure, though diffusive, spin current (i.e. not accompanied by charge motion). In our work, we show evidence of pure spin transport — an often sought-after goal for spin transport devices — across defect centers in diamond. Our measurements are performed on an ensemble containing fewer than 100 net spins under conditions where the thermally-averaged polarization and polarization gradient are vanishingly small. In contrast to non-equilibrium experiments, monitoring the 'spin noise' — stochastic, temporary deviations of the polarization which are "averaged out" in measurements of large ensembles — allows us to characterize the intrinsic spin dynamics of the ensemble [11].

For small spin ensembles, fluctuations become the key to not only measuring spin diffusion, but also modeling it. In macroscopic systems containing a large number of particles, Fick's law of diffusion describes the time evolution of particles moving from regions of high to low concentration, resulting in a smooth (i.e. fluctuation-free) transition toward equilibrium. By contrast, polarization in few-spin ensembles can instantaneously be much larger than the Boltzmann polarization, and even flow "against" the polarization gradient [12]. Our measurements are corroborated with a model which numerically simulates this inherent randomness of few-spin, statistically-polarized ensembles.

Spin centers in diamond have attracted much attention because of their long spin-lattice relaxation time, T_1 [13]. In order to study flip-flop-dominated spin dynamics, we have fabricated a nano-scale channel of implanted P1 centers in diamond at a density of 6 ppm. The flip-flop fluctuations are thereby constrained to this 'spin wire.' The density of P1 centers results in strong dipolar coupling between spins, and a spin-spin relaxation time, $T_2 = 6.7$ μs, which is many orders of magnitude shorter than $T_1 = 1.3$ s. Since the flip-flop time T_{ff} is equal to 30 T_2 [14], the spins in the wire undergo $\sim 10^4$ flip-flops for each T_1

relaxation event.

We use magnetic resonance force microscopy (MRFM) to probe the spins within the wire (Fig. 1a). The force detector is an IBM-style ultra-soft cantilever [15] with a $SmCo_5$ magnetic particle glued onto the tip. To resonantly detect spins, we implement the iOSCAR timing protocol [16]. A super-conducting niobium coil is used to drive the spin resonance at a frequency of $\frac{\omega}{2\pi} = 2.18$ GHz. This frequency defines a 'resonant slice' where the total magnetic field (tip field plus external field) experienced by sample spins is equal to $\frac{\omega}{\gamma} = 780$ G. By driving the cantilever at its self-determined resonant frequency to an amplitude of 150 nm, the resonant slice sweeps out a volume of the same width, hereafter termed the detection volume.

We scan the detection volume into the spin wire and measure the force exerted on the cantilever by the selected spins. From this measurement we can extract two quantities: spin signal (Fig. 1f, top), and correlation time (Fig. 1f, bottom). The spin signal is obtained from the variance in the time record of the force signal and is directly related to the number of measured spins [17]. The force correlation time, τ_m, describes the characteristic time for the net moment of the detected spins to decorrelate. Once the detection volume enters the channel, the spin signal grows with the number of detected spins, eventually reaching a plateau when completely within the wire. The correlation time shows more complex behavior as a function of walk-in distance. These results can be understood within the framework of flip-flop-mediated spin diffusion: ensemble correlation is lost as spin diffuses into or out of the detection volume. Just inside a displacement of 0 nm in Fig. 1b, the force signal fluctuates as spins inside the volume easily and rapidly flip-flop with outside neighbors, resulting in a relatively short correlation time. With increasing overlap of the detection volume and the spin wire, spin must diffuse further to exit the detection volume and change the overall state of the ensemble, thus increasing τ_m. The correlation time peaks when approximately 66 % of the detection volume has entered the channel. This is attributed to the force sensitivity profile of the detection volume: the middle of the volume is most sensitive to spins (indicated by red in Fig 1), while the edges are least sensitive (blue; see Sec. V). As the detection volume approaches 100 % overlap (at 150 nm), spins are able to diffuse out either side of the most sensitive (red) region, reducing the correlation time by roughly a factor of 2. Scanning deeper into the channel results in no further change, since the measurement geometry becomes translationally invariant.

A global measurement of the spin polarization, encompassing the entire spin wire, would not uncover this spin transport process. The correlation time τ_m plotted in Fig. 1f does not indicate the time scale over which global sample magnetization decays away, namely T_1; rather, the correlation time is dominated by spin transport out of our detection volume. As such, our measurement is similar to the determination of spin-lifetime by electrically-detected three-terminal Hanle or optically-detected "local Hanle" [18], both of which can be obscured by spins diffusing away from the detection volume (electrical contact or optical probe spot). However, in light of the long T_1 in our system, the flip-flop mechanism provides an efficient means of pure spin transport through the spin wire. In the limit of measuring a single spin, T_1-type relaxation would be indistinguishable from flip-flop induced polarization changes. We can distinguish these effects because we can systematically vary the size of the overlap of the detection volume with the spin wire, as well as the number of detected spins.

Since the polarization gradient vanishes at thermal equilibrium, application of a conventional model of diffusion driven by the polarization gradient would lead one to conclude that τ_m is independent of detection volume position within the wire. Such a model neglects the spin fluctuations which dominate for small ensembles. Therefore, in order to fit the measured data in Fig. 1f, we use a Monte Carlo simulation which simulates the flip-flops between individual spins as a Markov process. From this fit we can extract the flip-flop time T_{ff}, which we find to be 0.21 ms. Using the relationship $T_2 = \frac{T_{ff}}{30} = 6.7$ μs, we find good agreement with previous measurements of T_2 (10.4 ± 7.1 μs) [19]. The measured τ_m can be viewed as the time needed to

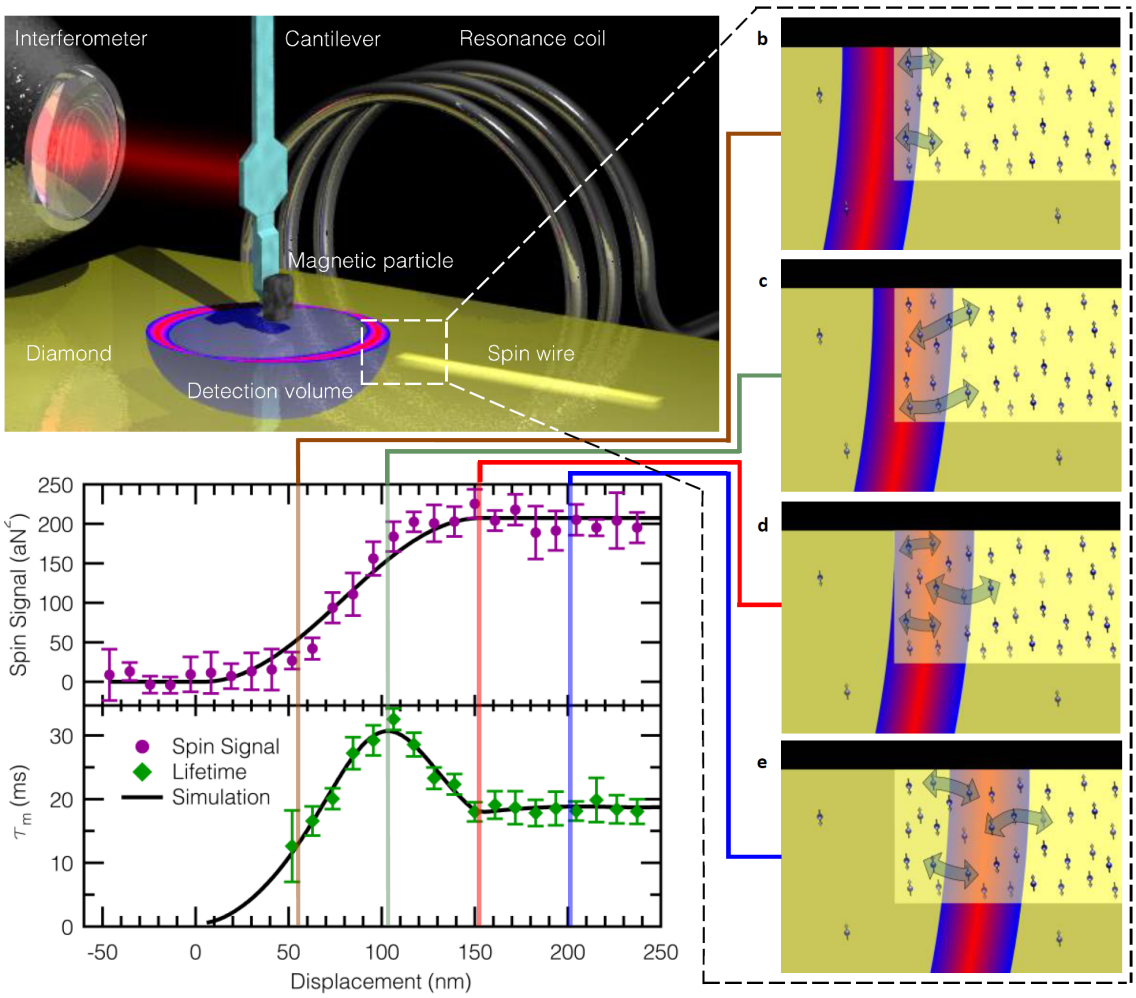

FIG. 1: **MRFM spin wire setup, scan zoom-ins, and spin wire measurements.** **a**, MRFM setup for measuring the 200 nm x 250 nm x 4 μm spin wire of P1 centers in diamond. The coil resonates spins along a contour of the magnetic particle's field called the 'resonant slice,' and as the cantilever oscillates, this slice sweeps out a spin detection volume. Spins toward the center of the detection volume contribute to the spin signal more strongly (red) than spins near the edge (blue). **b-e**, Zoom-ins showing the detection volume scanned into the stripe, and spins diffusing out. **f**, The spin signal as a function of walk-in distance increases until the volume is fully inside the spin wire. **g**, The correlation time of the measured spins. At first spins are able to quickly diffuse out of the volume, but as the measurement volume is walked in further, spins must diffuse a longer distance to exit the volume, causing the correlation time to increase. Once the measurement volume is fully inside the stripe, spins can diffuse out both sides, decreasing the correlation time to roughly half the peak value.

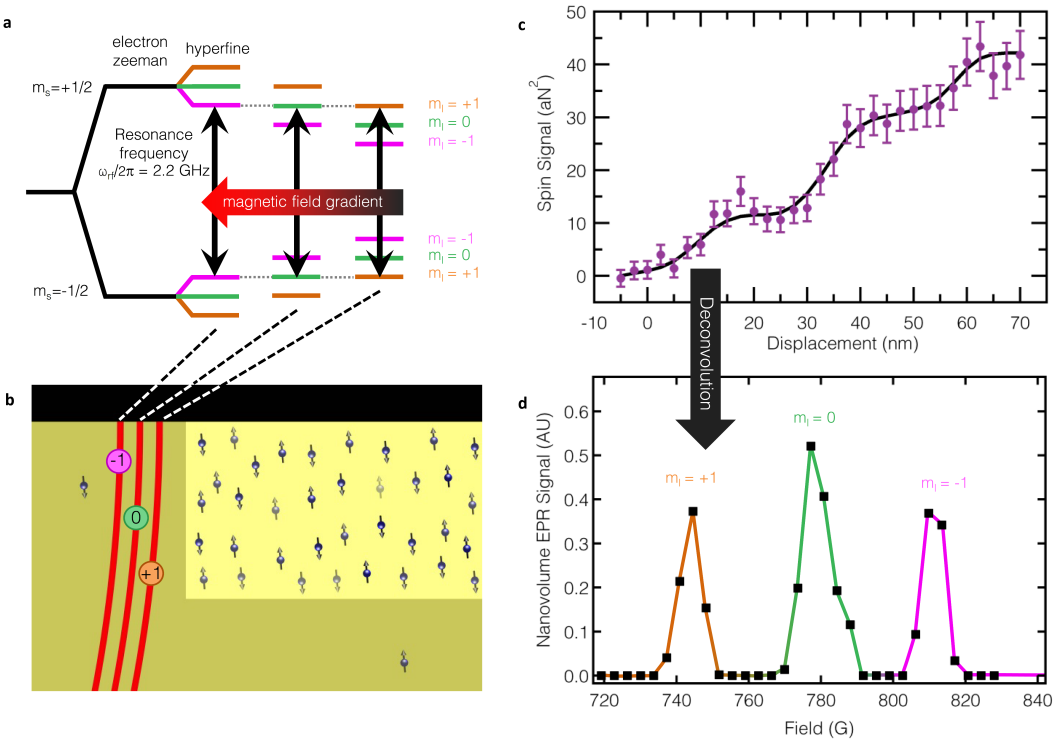

FIG. 2: **Hyperfine spectrum measurement for nanowire.** **a**, Energy level diagrams for three spin detection volumes resulting from the hyperfine splitting. The three nuclear spin populations (m_I = -1, 0, +1) are simultaneously on resonance, but due to the magnetic field gradient, this occurs at three distinct locations in the sample. **b**, The three volumes are slowly scanned into the spin wire, one at a time. **c**, The spin signal increases in a step-like fashion as each volume enters the wire with the solid line showing the weighted smoothing spile used for signal deconvolution used to obtain the force spectrum shown in **d**. **d**, A nanovolume EPR spectrum can be obtained from deconvolving the spin signal with the three hyperfine peaks of average FWHM of 7.6 Gauss resolved.

transport spin out of the detection volume via random-walk diffusion processes, with each step taking an average time of T_{ff}. From the measured flip-flop rate, we can extract a diffusion constant of $D = \frac{a^2}{T_{ff}} \approx 4.5 \times 10^{-9}\ \frac{\mathrm{cm}^2}{\mathrm{s}}$, where $a = 9.82$ nm is the average nearest-neighbor separation for spins in the 6 ppm wire. The diffusion length for a pure spin current can then be determined by $L = \sqrt{DT_1}$, for which we find 721 nm. This is competitive with metallic spin transport devices at room temperature [20].

Suppression of diffusion can occur when, due to a magnetic field gradient, neighboring spin sites experience different Zeeman splitting which would cause flip-flops to violate energy conservation [21, 22]. This mismatch in Zeeman splitting can be compensated if there is substantial variation of the spin-split levels throughout the sample. This variation is characterized by the ESR linewidth. We measure an inhomogeneously broadened linewidth of 7.6 Gauss as discussed below and in Sec. IV. This linewidth is significantly broader than those which have been observed in other MRFM spectroscopy experiments, and therefore we do not observe suppression of diffusion in our experiment.

Next, we repeat the experiment with a variation of the iOSCAR protocol in order to simultaneously improve spatial resolution and preserve maximum force sensitivity. A conventional iOSCAR measurement utilizes the entire detection volume swept out by the cantilever oscillation (red and blue regions, Fig. 1b-e), as this couples to the largest number of spins and creates the largest force signal. By truncating the detection volume to the most-sensitive (red) portion, we couple only to spins in this smaller region while maintaining high force sensitivity. In contrast, reducing the cantilever oscillation amplitude, while similarly improving resolution, simply compresses the sensitivity profile by shrinking the red region and retaining the reduced sensitivity near the edges. Utilizing this technique (see Sec. V), which we call partially-interrupted OSCAR (piOSCAR), we again scan the detection volume into the spin wire. The improved resolution enables us to resolve a staircase structure with three steps (Fig. 2c), corresponding to hyperfine splitting as discussed below.

The P1 center is a substitutional nitrogen defect with an unpaired spin-$\frac{1}{2}$ electron and spin-1 nucleus. Due to hyperfine interaction, each Zeeman-split electron energy level splits into three states (Fig. 2a) that correspond to the three states for the nuclear spin, $m_I = -1, 0, 1$. The hyperfine splitting for our diamond crystal orientation with respect to the external field is 33 G [23]. In the approximately dipolar field of our probe magnet, this splitting manifests itself as three non-overlapping spin detection volumes, with each volume defined by the contour of magnetic field which satisfies the resonance condition for one hyperfine transition (Fig. 2b). We observe a step-like increase in the spin signal as each volume enters the wire and the cantilever becomes coupled to an additional hyperfine transition. The broadening of the steps' rising edges is caused by the width of each volume (b = 15 nm). The spacing between step edges (s = 25 nm), along with the hyperfine splitting constant (33 G) provides a means of measuring the MRFM probe field gradient, G = 1.3 G/nm. The staircase structure is a convolution of the implanted channel profile (essentially a step function), our force sensitivity profile, and the intrinsic ESR spectrum of spins in the sample. We can therefore obtain the ESR spectrum through the appropriate deconvolution steps (see Sec. IV). This spectrum is shown in Fig. 2d.

Our measurements demonstrate that both spin transport and spectroscopic information can be obtained by observing spin fluctuations about the equilibrium in a nano-scale diamond spin wire. We are able to distinguish spin transport from T_1-type spin relaxation. We find a flip-flop time T_{ff} of 0.21 ms and determine a spin diffusion constant of $D \approx 4.5 \times 10^{-9}$ $\frac{\mathrm{cm}^2}{\mathrm{s}}$, for 6 ppm P1 centers in diamond. This regime — small spin ensembles which experience substantial spin-spin coupling — could prove useful for the development of spintronic technologies, especially as technology trends towards ever-smaller devices. Additionally, the capability to spatially resolve nuclear spin states might allow for the selective study of nuclear spin dynamics via electron spin detection in a manner reminiscent of bulk electron-nuclear double resonance (ENDOR), but at the nano-scale. In all, our measurements elucidate the mechanisms of spin transport in small ensembles, and are a valuable tool for the study of nano-scale spin phenomena and devices.

Methods The ultra-soft silicon cantilever has a spring constant of 100 μN/m, resonance frequency of about 3 kHz, and approximate dimensions of 90 microns in length, 1 micron width, and 100 nm thickness. Displacement of the cantilever is measured through a 1550 nm laser interferometer. The MRFM measurements were taken at temperatures of 4.2 K. The measured moment of the $SmCo_5$ magnetic particle was 3.6×10^{-12} J/T. The niobium resonator coil had about 2.5 turns and a 300 micron diameter, and the resonance bowl had a diameter of about 3 microns. The diamond sample studied in this experiment had a background nitrogen concentration of 0.3 ppm (5.27×10^{16} cm^{-3}). To create the high spin-density wire, the sample was first prepared using electron beam patterning and then exposed to nitrogen ion implantation at a variety of energies to create a uniform spin density. Finally the sample was annealed to yield an approximately uniform,

channel (6 ppm or 1.06×10^{18} cm^{-3}) with width, depth, and length of 200 nm, 250 nm, and 4 microns, respectively. The sample was purchased commercially from Element Six, grown via chemical vapor deposition, and the nitrogen ion implantation was performed by Leonard Kroko Inc.

III. MICROSCOPIC MONTE CARLO SIMULATION OF SPIN DIFFUSION IN QUASI 1D SYSTEMS

To fit our data, we developed a Monte Carlo simulation of spins flip-flopping according to the random-walk dynamics as originally introduced by Bloembergen, and discussed by Abragam [14]. In the experiment, we are only sensitive to changes in magnetization along the x-direction, defining x to be along the wire, which led us to implement a one-dimensional simulation for computational efficiency. In our simulation we break up the spin wire into an array of spins, then let the spins randomly walk. We make the approximation that all spins can flip with neighbors that are located at an arbitrary θ and ϕ, referring to spherical coordinates, and take the projection along the x-axis for each flip-flop event; thus if an up spin flip-flops to a nearest neighbor (6 ppm $\Leftrightarrow$ 9.82 nm nearest neighbor separation) at an angle of $\theta = 45°$, $\phi = 0$, then we are only interested in the x-component of $r \sin\theta \cos\phi = 9.82 \sin(45°) \cos(0) = 9.82/\sqrt{2}$ nm, which we use to calculate the change in the spatial distribution of spin (magnetization). This approximation is valid in the limit that the discrete θ and ϕ imposed by the crystal lattice become negligible; since the lattice constant for diamond is 3.57 Å, adjacent lattice sites differ by about 2 degrees (from a distance away of 9.82 nm), which we consider a discretization that is small enough to ignore. A further consideration with this approximation is that spins on the edges of the wire have less neighbors, and thus cannot flip-flop at any arbitrary θ or ϕ. As a consequence of having less neighbors, these edge spins flip-flop less frequently, and since there are significantly less of them than interior spins, we also consider their effects small enough to ignore.

The random walk dynamics in our model require a step size, and a rate at which to take the steps. The step size for our system is the average nearest-neighbor separation, which has large variation given the fact that the nitrogen atoms end up on random lattice sites during implantation. Despite this variation in nearest-neighbor separation, which causes more closely-packed spins to flip-flop more rapidly, and more isolated spins to flip-flop less rapidly, the average flip-flop rate for spins is given by $W = \frac{1}{30T_2} = 3.2$ kHz. This gives the average flip-flop time $T_{ff} = \frac{1}{W}$, for the time-random flip-flop transitions modeled in the simulation. This treatment of the flip-flop time avoids the computationally prohibitive alternative of calculating the flip-flop rate between all pairs of spins.

Conceptually, we represent a flip-flop event by having a single spin hop, instead of having two neighboring spins undergo simultaneous transition flips, which is a way of increasing computational efficiency by using half the number of spins to accurately represent the magnetization record of all the spins. This can be thought of as shifting the value of magnetization for all spins up by a Bohr magneton — setting down spins to having zero moment, and up spins to 2 μ_B — because when an actual flip-flop occurs, there is the transport of 2 μ_B along the direction of the vector connecting the two spins. Whereas our measurement fluctuates about zero net moment with roughly $\frac{N}{2}$ spins up and $\frac{N}{2}$ spins down (where N is the number of spins that we measure), our simulation fluctuates about an average moment of $\frac{N}{2} \times (2\mu_B) = N\mu_B$, which is an offset that we subtract off to obtain the magnetization record.

To simulate the dynamics, we generate a Markov matrix that contains the probabilities that a given spin transitions from a particular spatial bin (represented by a column of the matrix) to a particular spatial bin (rows of the matrix) in a time interval Δt. For example, a spin in the middle of the wire can flip-flop a distance of 9.82 nm in any direction, at an average rate W, corresponding to a total probability of hopping in a time Δt of $P = W\Delta t$. To eliminate the chance of an individual spin undergoing two or more flip-flops in the time interval, the con-

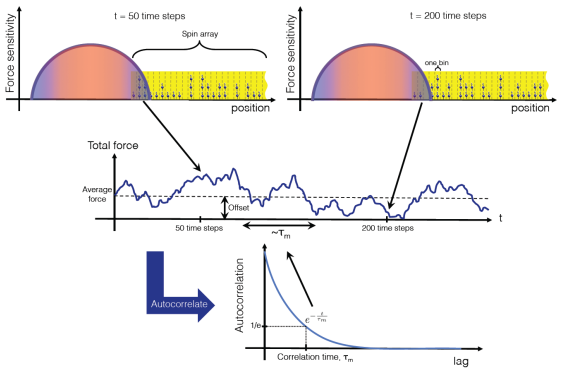

FIG. 3: Schematic illustration of the simulation. As depicted, the detection volume has walked in three steps, and measures the first three bins of the spin array. The spins randomly walk throughout the array resulting in time dependent total force. Autocorrelation of the force gives the spin correlation time for the given location of the detection volume.

dition $P \ll 1$ must be satisfied. We take only the x-component of the hop, which must be discretized into bins: given that the spins can hop in any direction with equal probability, the probability distribution for the x-component is a flat distribution out to the nearest-neighbor separation. Thus, for constructing the elements (probabilities) of the Markov matrix we have for each element one of three cases: 1.) the value of the element is 0 because it belongs to a spatial bin that is too far away (> 9.82 nm) for the spin to hop, 2.) the element is equal to $p = \frac{P}{N_{lb}}$ where $N_{lb} = (\frac{2\times 9.88\,\mathrm{nm}}{\text{bin size in nm}})$ is the number of local bins that are 'within reach', 3.) the element is on the diagonal and is thus 1 minus the sum of the other values in the column. The values of the diagonals are chosen such that the columns are properly normalized, where the total probability of the spin to go somewhere (including staying in its current bin) is unity.

The magnetization array divides the wire into a number of bins of finite size Δx, such that there are only a few net spins in each bin. As an approximation, we take the center of the bin to be the location of all the spins in the region that the bin represents, which becomes more accurate as the bin size gets smaller. We let the spins in our array propagate in time according to the described dynamics, generating a new magnetization record for each small time step Δt. To simulate our experimental measurement of walking into the wire, we multiply the magnetization array by our spin sensitivity profile (as described in Sec. V, with units of $\frac{\text{force}}{\text{moment}}$): in the first step we multiply the first bin in our magnetization array by the leading edge of the sensitivity profile, followed by multiplying the first two bins by the corresponding sensitivity, and so on and so forth, resulting in a force record ($\frac{\text{force}}{\text{moment}} \times \text{moment} = \text{force}$) for each step into the wire. To extract the correlation time, we take the autocorrelation of the force record and fit a decaying exponential; the exponential's time constant is the correlation time. Fitting a decaying exponential to the autocorrelation assumes that the flip-flops can be modeled as a Poisson random process where the probability P for a flip-flop to occur is the same for every time step Δt. Typical parameters for the simulation used to fit the data are: Number of Δt time steps$\sim 10^7$, flip-flop probability $P \sim 0.02$, and $\Delta x \sim 3$ nm.

IV. SPECTROSCOPIC MEASUREMENTS ON NANOSCALE VOLUME

The data presented in Fig. 2c shows the ESRFM force recorded as the cantilever with a probe magnet is brought closer to the end of the ion implanted spin nanowire. The distinctive staircase-shaped pattern of increasing force signal, observed in the data, is consistent with the three individual sensitive volumes, defined by the splitting of the ESR line by the hyperfine interaction given by Eq. 1, entering, consecutively, the end of the nanowire. The obtained data, combined with our knowledge of the spatial distribution of the spins in the nanowire and the spatial width of the *rf* interrupt (see Sec. V) allows us to extract spectroscopic information about the spins in the nanowire.

The Hamiltonian for an electron on a P1 center has four terms: electron Zeeman, hyperfine

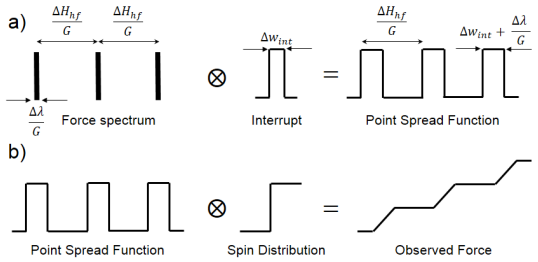

FIG. 4: Schematic representation of a two-step formation of the force signal shown in Fig. 2c. a) A hyperfine split spectrum of an electron on a P1 center results in spatial force spectrum consisting of three sensitive slices of spatial width of $\Delta\lambda/G$, where $\Delta\lambda$ is the ESR linewidth and G is the magnetic field gradient, which are spatially separated by $\Delta H_{hf}/G$, where ΔH_{hf} is the hyperfine splitting of the spectrum. The force spectrum convolved with the shape of the interrupt, incorporating cantilever oscillation and microwave manipulation, as described in Sec. V, forms the Point Spread Function (PSF) of the ESRMRF. b) The convolution of the PSF with the step function-like spatial distribution of the spins in the nanowire results in the observed, staircase shaped force pattern shown in Fig. 2c.

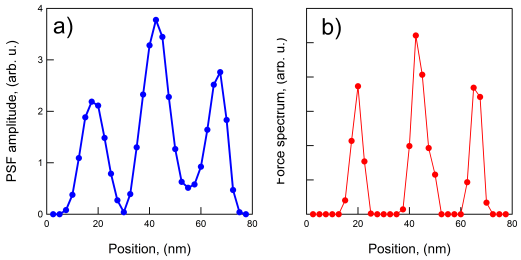

FIG. 5: a) ESRFM point spread function (PSF) recovered via deconvolution of the force signal shown in Fig. 2c with the step function-like spatial distribution of the spins in the nanowire. b) Spatial representation of the force spectrum of electron spins on P1 center in diamond recovered via deconvolution of the PSF with the shape of a 15 nm interrupt.

interaction, quadrupole, and nuclear Zeeman,

$$\mathcal{H} = \underbrace{g_e\mu_B\vec{S}\cdot\vec{H}}_{\substack{\text{Electron}\\ \text{Zeeman}}} + \underbrace{A\vec{S}\cdot\vec{I}}_{\text{Hyperfine}} + \underbrace{PI_z^2}_{\text{Quadrupole}} - \underbrace{g_n\mu_n\vec{I}\cdot\vec{H}}_{\substack{\text{Nuclear}\\ \text{Zeeman}}} \quad (1)$$

where g_e and g_n are the electron and nitrogen nucleus$g$-factors, μ_B and μ_n are the Bohr magneton and nuclear magneton respectively, S and I are the spin of the electron and nucleus, and H is an externally applied magnetic field. The hyperfine term of the Hamiltonian is responsible for the splitting of the ESR spectrum into three lines separated by the hyperfine splitting ΔH_{hf} = 33 Gauss.

The general principle of the formation of the observed force pattern is shown schematically in Fig.4. The force pattern formation occurs in two steps. A hyperfine split spectrum of an electron on a P1 center results in spatial force spectrum (see Fig.4a) consisting of three sensitive slices of spatial width of $\Delta\lambda/G$, where $\Delta\lambda$ is the ESR linewidth and G is the magnetic field gradient, which are spatially separated by $\Delta H_{hf}/G$, where ΔH_{hf} is the hyperfine splitting of the spectrum. The force spectrum convolved with the shape of the interrupt, incorporating cantilever oscillation and microwave manipulation, as described in Sec. V, forms the Point Spread Function (PSF) of the ESRMRF. Subsequently, the convolution of the PSF with the step function-like spatial distribution of the spins in the nanowire results, as illustrated in Fig.4b, in the observed, staircase shaped force pattern shown in Fig. 2c.

Based on the described model, we have extracted the shape of the electron spin spectrum in the implanetd nanowire using the known shape of the interrupt and the good knowledge about the spatial distribution of spins in the nanowire with the result shown in Fig. 5b. This was achieved via two-step deconvolution process. In the first step, the experimental data approximated by a weighted smoothing spine fit, shown in Fig. 2c, is deconvolved with a step step function, approximating the spatial spin distribution, resulting in the PSF shown in Fig. 5a. The deconvolution was done numerically, using a modified Van-Cittert iterative procedure of deconvolution. During the second step, the obtained PSF is deconvolved

with the interrupt shape approximated by a 15 nm wide square pulse resulting in the force spectrum shown in Fig. 5b. This deconvolution was done using iterative Bayesian-based method [24]. The resulting spectral linewidth of 7.6 Gauss, is attributed to the inhomogenious line broadening and an therefore contributes to the explanation of the absence of suppression of spin diffusion in our experiment even in the presence of the strong magnetic field gradient.

V. PARTIALLY INTERRUPTED IOSCAR PROTOCOL

We implemented a slightly modified version of the iOSCAR protocol which improves spatial resolution, which we call partially-interrupted oscillating cantilever-driven adiabatic reversals, or pi-OSCAR. The iOSCAR protocol involves periodically interrupting the microwave power for a half cantilever cycle, which causes the orientation of spins in the measurement volume to change by 180 degrees with respect to the cantilever motion. This in turn causes the sign of the force on the cantilever to be periodically reversed, which can then be demodulated via a lock-in amplifier to obtain the spin signal. The use of a lock-in allows for increased spin sensitivity. The modification we implement in pi-OSCAR is to interrupt the microwave power for *less* than a half cantilever cycle, about the center of the cantilever's motion. Since only the spins that are periodically interrupted contribute to the spin signal due to the lock-in detection, by decreasing the width of the interrupt it correspondingly decreases the measurement volume width. Using this modification, we get larger signals from the same measurement volume compared to iOSCAR, enabling us to probe down to smaller measurement volumes before we become limited by noise. The larger signal is due to the fact that the center of the spin detection volume has a larger force sensitivity per spin than the edges of the volume. The following derivation solves for the force sensitivity of the detection volume as a function of lateral position within the volume for the standard iOSCAR protocol measurement. From this iOSCAR sensitivity profile we can then show how implementing partial interrupts in pi-OSCAR results in greater spin sensitivity per unit volume for small detection volumes.

We treat the cantilever in our experiment as a simple damped, driven harmonic oscillator with spring constant k, viscous damping coefficient c, effective mass m, and driving force $F(t)$. From Newton's second law we have

$$m\ddot{x} = F(t) - kx - c\dot{x} \tag{2}$$

which can be rewritten in a more conventional form:

$$\ddot{x} + 2\Gamma\omega_0\dot{x} + \omega_0^2 x = \frac{F(t)}{m} \tag{3}$$

where the damping ratio is $\Gamma = \frac{c}{2\sqrt{mk}}$ and the undamped angular frequency is

$$\omega_0 = 2\pi f = \sqrt{\frac{k}{m}} \tag{4}$$

Driving the cantilever results in a steady state oscillation such that the energy dissipated each cycle is supplied by $F(t)$ (in accordance with its quality factor). Thus the position of the cantilever's magnetic tip is given by

$$x_c(t) = x_{pk}\sin(\omega_c t) \tag{5}$$

where $\omega_c = 2\pi f_c$ is the steady state cantilever frequency and x_{pk} is the cantilever peak oscillation amplitude. Now, as the cantilever oscillates, the resonance bowl sweeps past spins within the spin detection volume and causes them to adiabatically invert. This results in the spin's magnetic moment $\vec{m}$ to vary as a pulse wave in time:

$$\vec{m}(t) = \mu_B f_{pulse}(t) \tag{6}$$

here, μ_B is a Bohr magneton and $f_{pulse}(t)$ is a pulse wave modultion signal with a pulse period

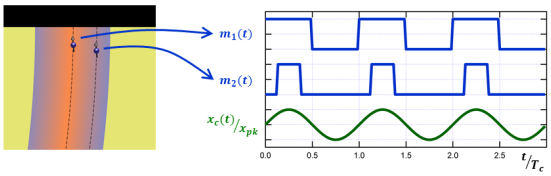

FIG. 6: Pulse function of two spins' moments at different locations in the detection volume.

(width) T_{pulse} and unit amplitude:

$$f_{pulse}(t) = \begin{cases} 1 & \text{for } T_c' - \frac{T_{pulse}}{2} < t < T_c' + \frac{T_{pulse}}{2} \\ -1 & \text{otherwise} \end{cases} \tag{7}$$

where $T_c' = T_c(\frac{1}{4} + m)$ and $m = 0, 1, 2, 3...$ and $T_c = \frac{1}{f_c}$ is the cantilever period. For a spin in the center of the detection volume this results in a 50% duty cycle pulse wave (i.e. a square wave with $T_{pulse} = \frac{T_c}{2}$) modulation of the spin's moment $\vec{m}$ with a period equal to that of the cantilever, and for spins not in the center, the pulse is greater or less than a 50% duty cycle (see Fig. 6). Because it is the cantilever's magnetic tip that cause the spins to invert, the pulse wave modulation is necessarily phase-locked and frequency-locked to the cantilever motion. This modulation of $\vec{m}$ provides a small additional driving force on the cantilever $F_{spin}(t) = |\vec{\nabla}(\vec{m}(t) \cdot \vec{B})| = G\mu_B f_{pulse}(t)$, where $\vec{B}$ is the magnetic field from the cantilever tip and G is appropriate magnetic field gradient, which we take to be uniform within the shallow spin wire. Adding this additional force to eq. 9 and plugging in the steady state solution from eq. 5 yields:

$$-x_{pk}\omega_c^2 \sin(\omega_c t) + 2\Gamma x_{pk}\omega_0\omega_c \cos(\omega_c t) + \omega_0^2 x_{pk} \sin(\omega_c t) = \frac{F(t)}{m} + \frac{F_{spin}(t)}{m} \tag{8}$$

but since $F_{spin}(t)$ is a pulse wave modulation that is frequency and phase locked to the oscillation of the cantilever, and because the cantilever itself shows sensitive response only near its resonant frequency (for high quality factor), we can keep only the Fourier series component of $F_{spin}(t)$ at the cantilever frequency ω_c. This gives:

$$-x_{pk}\omega_c^2 \sin(\omega_c t) + 2\Gamma x_{pk}\omega_0\omega_c \cos(\omega_c t) + \frac{k}{m} x_{pk} \sin(\omega_c t) = \frac{F(t)}{m} + \frac{G\mu_B}{m} b_1 \sin(\omega_c t) \tag{9}$$

where b_1 is the dimensionless amplitude of the Fourier component of interest (defined below). Note that the 3rd term on the l. h. s. can be grouped with the 2nd term on the r. h. s.:

$$-x_{pk}\omega_c^2 \sin(\omega_c t) + 2\Gamma x_{pk}\omega_0\omega_c \cos(\omega_c t) + [k - \frac{G\mu_B b_1}{x_{pk}}]\frac{x_{pk}}{m} \sin(\omega_c t) = \frac{F(t)}{m} \tag{10}$$

This demonstrates that the modulation of the spin effectively results in a small shift δk in the cantilever's spring constant:

$$\delta k = \frac{G\mu_B b_1}{x_{pk}} \tag{11}$$

From the undamped angular frequency eq. 4, we find for small changes in the spring constant δk:

$$\frac{\delta f}{\delta k} = \frac{1}{4\pi m}\sqrt{\frac{m}{k}} = \frac{1}{2k}(\frac{1}{2\pi}\sqrt{\frac{k}{m}}) \tag{12}$$

and upon substitution back into eq 4 this gives a well known result which shows that small changes in the spring constant give a linear response to changes in the oscillator's frequency:

$$\frac{\delta f}{f} = \frac{1}{2}\frac{\delta k}{k} \tag{13}$$

Now we need to find the Fourier component b_1 for a given spin (not necessarily in the center of the volume). First, we define the Fourier series of a given function $f(t)$ with period T:

$$f(t) = a_0 + \sum_{n=1}^{\infty} \left(a_n \cos(\frac{2\pi nt}{T}) + b_n \sin(\frac{2\pi nt}{T}) \right) \tag{14}$$

and Fourier coefficients:

$$a_0 = \frac{1}{T} \int_{-T/2}^{T/2} f(t)dt \tag{15}$$

$$a_n = \frac{2}{T} \int_{-T/2}^{T/2} f(t) \cos(\frac{2\pi nt}{T})dt \tag{16}$$

$$b_n = \frac{2}{T} \int_{-T/2}^{T/2} f(t) \sin(\frac{2\pi nt}{T})dt \tag{17}$$

where $f(t)$ in this case is the pulse modulation of the spin $f_{pulse}(t)$. By plugging eq. 7 into eq. 17 and calculating a straightforward integration we can solve for b_1 as a function T_{pulse}:

$$\begin{aligned} b_1(T_{pulse}) = & \\ & = \frac{2}{T} \int_{-T/2}^{T/2} f(t) \sin(\frac{2\pi t}{T})dt \\ & = \frac{4}{\pi} \sin(\frac{T_{pulse}}{T_c}\pi) \end{aligned} \tag{18}$$

Fig. 7 shows b_1 as a function of T_{pulse}.

Having found $b_1(T_{pulse})$, we now need to relate the pulse wave of a given spin to its lateral location x_s within the detection volume. Let $x_s = 0$ be the center of the detection volume (i. e. the location of the resonant slice when the cantilever is at its equilibrium position). From eq. 5 the range of x_s is: $-x_{pk} < x_s < x_{pk}$. We note that the time t_{flip} at which the spin will flip as a function of its location x_s can be found by equating $x_s = x_{pk} \sin(2\pi f_c t_{flip})$ which

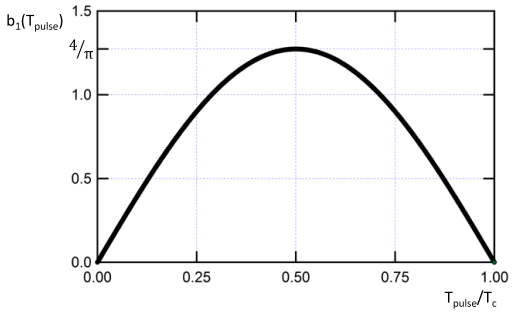

FIG. 7: First harmonic Forier series amplitude b_1, as a fuction of moment pulse width.

gives $t_{flip} = \frac{T_c}{2\pi} \arcsin(\frac{x_s}{x_{pk}})$. However, the function $\arcsin(x)$ has a restricted range $-\frac{\pi}{2} < x < \frac{\pi}{2}$ as a consequence of satisfying the vertical line test for a well defined (one-to-one mapped) function. As a consequence of this we need to pick up the 'other' solution (sometimes referred to as the geometric reflection), and the spacing between these solutions gives the pulse width. Since the other solution is symmetric about $\frac{\pi}{2}$, where $\frac{\pi}{2}$ corresponds to one fourth of the cantilever period, we can write the pulse width as $T_{pulse}(x_s) = 2(\frac{T_c}{4} - \frac{T_c}{2\pi} \arcsin(\frac{x_s}{x_{pk}})) = T_c(\frac{1}{2} - \frac{1}{\pi} \arcsin(\frac{x_s}{x_{pk}}))$.

$$\begin{aligned} T_{pulse}(x_s) = & \\ & = 2(\frac{T_c}{4} - \frac{T_c}{2\pi} \arcsin(\frac{x_s}{x_{pk}})) \\ & = T_c(\frac{1}{2} - \frac{1}{\pi} \arcsin(\frac{x_s}{x_{pk}})) \end{aligned} \tag{19}$$

Having solved for T_{pulse} as a function of spin location x_s, we can now combine eqs. 18 and 19 to give $b_1(x_s)$:

$$b_1(x_s) = \frac{4}{\pi} \sin(\frac{\pi}{2} - \arcsin(\frac{x_s}{x_{pk}})) \tag{20}$$

Since the b_1 coefficient of a detected spin is proportional to the frequency shift of the cantilever due to that spin (eqs. 11 and 13) we have:

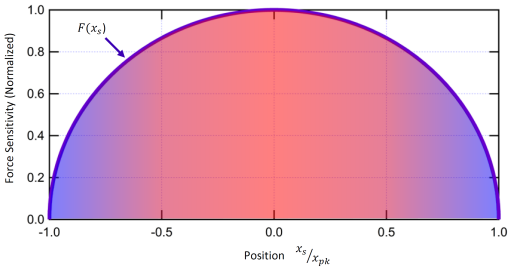

FIG. 8: Force sensitivity profile of spin detection volume as a function of lateral location.

$$\delta f(x_s) = \frac{2G\mu_B f_c}{\pi x_{pk}} \sin(\frac{\pi}{2} - \arcsin(\frac{x_s}{x_{pk}})) \quad (21)$$

We see that $b_1(0) = \frac{4}{\pi}$ for a spin in the center of the detection volume, which gives the frequency shift:

$$\delta f = \frac{2G\mu_B f_c}{\pi k x_{pk}} \quad (22)$$

Although we use frequency detection in our measurements and therefore δf is a useful quantity, it is often more useful to report the corresponding forces that are detected from the spins acting on the cantilever. Therefore, we can convert back to force via Hooke's law ($F = \delta k \cdot x_{pk}$) where x_{pk} is used to yield the peak force and δk is given by eq. 11 which gives the force sensitivity per spin of the detection volume as a function of lateral position.

$$F(x_s) = G\mu_B \left[\frac{4}{\pi} \sin\left(\frac{\pi}{2} - \arcsin\left(\frac{x_s}{x_{pk}}\right)\right)\right] \sim 1 \text{ aN} \quad (23)$$

Having found the force sensitivity of the iOSCAR protocol, we can consider the modification of this in pi-OSCAR. The partial interruptions in the pi-OSCAR protocol result in a truncated force sensitivity, since only spins that are interrupted contribute to force detection (see Fig. 9). This provides an oportunity for increasing the force sensitivity of small detection volumes. Typically, in the iOSCAR protocol, smaller volumes are probed by decreasing the cantilever oscillation amplitude, and thus shrinking the entire force sensitivity profile (Fig. 10). With pi-OSCAR, the canntilever oscillation amplitude is kept at a large fixed value, and the volume is decreased by applying partial interruptions to the microwave resonator, and thus truncating the sensitivity profile (Fig. 10). This results in relatively large force sensitivity for small detection volumes. In the small detection volume regime, pi-OSCAR results in a $\left(\frac{4}{\pi} - 1\right) \rightarrow 27\%$ increase in the measured spin signal versus iOSCAR.

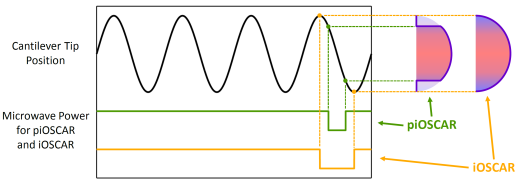

FIG. 9: Comparison of iOSCAR and piOSCAR rf pulse signals and the resultying force sensitivity profile.

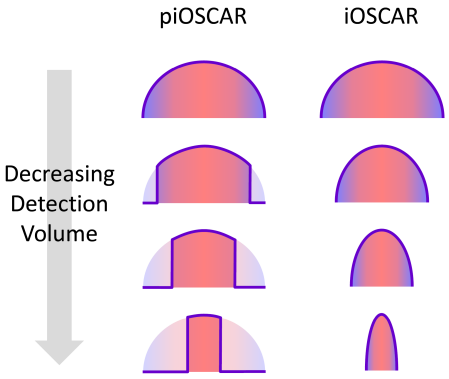

FIG. 10: Comparison of iOSCAR and piOSCAR for decreased detection volume width.

VI. IMPROVEMENT OF PERFORMANCE OF ESR MRFM APPARATUS

Improvement of force detection sensitivity of our MRFM apparatus is an ongoing effort in our drive towards detecting magnetic resonance signal from a single *nuclear* spin. We have already demonstrated EPR MRFM detection with signal sensitivity corresponding to $\sim$ 1–2 *electron* spins. Detection of a single *nuclear* spin will require improvement in force detection sensitivity by three orders of magnitude. Routes toward this goal include improvements in the optical interferometric cantilever displacement detection and reduction of the cantilever thermal noise. Our effort in these directions is described below.

A. Optical displacement detection

The displacement of a micromechanical cantilever detected by fiber-optic interferometry measures the interference between two laser beams one of which is reflected off the end of the optical fiber and a second reflected back into the optical fiber by the reflective surface of the cantilever. The visibility V characterizing the relative intensities of the two beams is given by:

$$V = \frac{R_f R_c}{R_f + R_c}, \tag{24}$$

where R_f is the fraction of power reflected at the end of the fiber and R_c is the fraction of power reflected at the cantilever. The visibility is a parameter of critical importance due to the fact that the shot nose spectral density $S_{\rm shot}$ of displacement detection, a quantity limiting detection sensitivity, depends on visibility as

$$S_{\rm shot} \sim \frac{1}{V}. \tag{25}$$

Thus, increasing V improves sensitivity. We have concentrated significant effort to improving cantilever visibility. By using various engineering measures including uses of similar materials in apparatus construction to minimize thermal drift and by improving procedures for doing cantilever-fiber alignment we were able to increase cantilever visibility from routinely achieved 4% to 70%. The result of this improvement is presented in Fig. 11 showing MRFM force noise as a function of signal modulation frequency recorded for two values of cantilever visibility. It can be seen that the onset of the shot noise shifts from $\sim$ 4 Hz to $\sim$ 40 Hz as visibility increases. The overall reduction of the thermal noise floor at low frequencies from $\sim$ 20 aN/$\sqrt{\rm Hz}$ to $\sim$ 10 aN/$\sqrt{\rm Hz}$ is due to improved quality factor Q of the MRFM cantilever that will be discussed further. The shift of the onset of the short noise allows modulation of MRFM signal at higher frequencies which avoids the low frequency $1/f$ noise which grows as the tip approaches the sample.

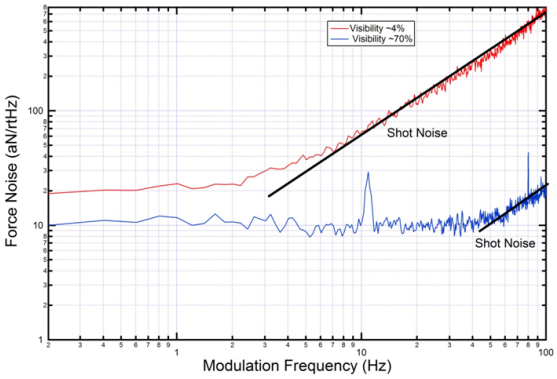

FIG. 11: MRFM force noise as a function of signal modulation frequency recorded for two values of cantilever visibility. It can be seen that the onset of the shot noise shifts from $\sim$ 4 Hz to $\sim$ 40 Hz as visibility increases. The overall reduction of the thermal noise floor at low frequencies from $\sim$ 20 aN/$\sqrt{\rm Hz}$ to $\sim$ 10 aN/$\sqrt{\rm Hz}$ is due to improved quality factor Q of the MRFM cantilever.

B. Reduction of cantilever thermal noise by increasing quality factor Q

The ultimate sensitivity limit for mechanical force detection is imposed by the thermal noise of the mechanical cantilever used for force detection.

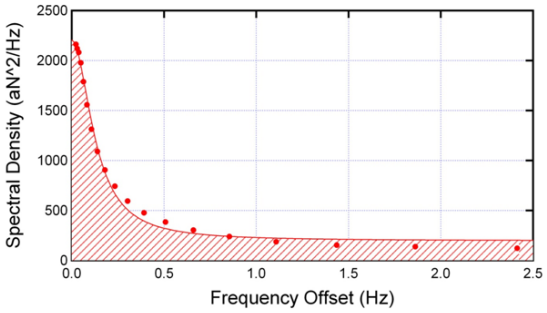

FIG. 12: Measured EPR signal spectral density using MRFM iOSCAR protocol with the modulation frequency of 75 Hz. The signal lifetime $\tau_m = 1.24\ s$ is measured from the signal linewidth. The are under the signal curve is proportional to the number of spins N participating in the interaction. The observed signal corresponds to $N = 13$ spins. The signal is much larger than the experimental noise floor.

The resulting thermal force noise F_{th} (in units of $\mathrm{N}/\sqrt{\mathrm{Hz}}$) depends on the cantilever quality factor Q as:

$$F_{th} \sim \frac{1}{\sqrt{Q}}. \tag{26}$$

Thus the thermal noise floor of the MRFM cantilever can be reduced by increasing Q. While there are multiple mechanisms that degrade Q, one of particular importance when the cantilever approaches the sample is cantilever surface contamination and electric charge trapping. To reduce the influence of these effects we have:

- Improved the process of gluing a probe micro magnet on the cantilever
- Changes to the procedure for shaping the probe micro magnet with the Focused Ion Beam (FIB)
- Improved methods of handling and storing the cantilever
- Improved the design of the cryogenic apparatus to minimize contamination

These measures were developed through interactions with our collaborators at UIUC. The resulting improvement of the cantilever thermal force noise by a factor of ~ 2 is shown in Fig. 11.

C. Verification of MRFM apparatus performance

Having implemented the improvements to MRFM signal detection described above, we have conducted a series of experiments verifying the performance of the MRFM apparatus. These experiments were also necessitated by the temporary shut-down of the research program in the first half of 2009 and the loss of the personnel associated with the project. The experiments were conducted on the standard γ-irradiated silica sample with the resulting density of E' centers of 6×10^{17} cm^{-3}. These results are shown in Fig. 12 which presents measured EPR signal spectral density using MRFM iOSCAR protocol with the modulation frequency of 75 Hz. The signal lifetime $\tau_m = 1.24$ s is measured from the signal linewidth. The are under the signal curve is proportional to the number of spins N participating in the interaction. The observed signal corresponds to $N = 13$ spins. The signal is much larger than the experimental noise floor. This result demonstrates force detection sensitivity sufficient for our research program including ENDOR MRFM detection.

VII. PREPARATION OF CUSTOM N-IMPLANTED DIAMOND SAMPLES FOR HIGH SENSITIVITY/RESOLUTION ESR MRFM IMAGING

At present there are only two large manufactures of synthetic single crystal bulk diamond suitable for scientific research: Element 6 [25] and Sumitomo [26]. Both companies grow diamonds via either a high pressure and high temperature (HPHT) method simulating the growth conditions of natural diamond but at a faster rate or via chemical vapor deposition (CVD). Chemical vapor deposition method of growth creates diamond crystals that are of very high purity. Typically, CVD diamond samples from these two companies contain less than 1 part per million (1

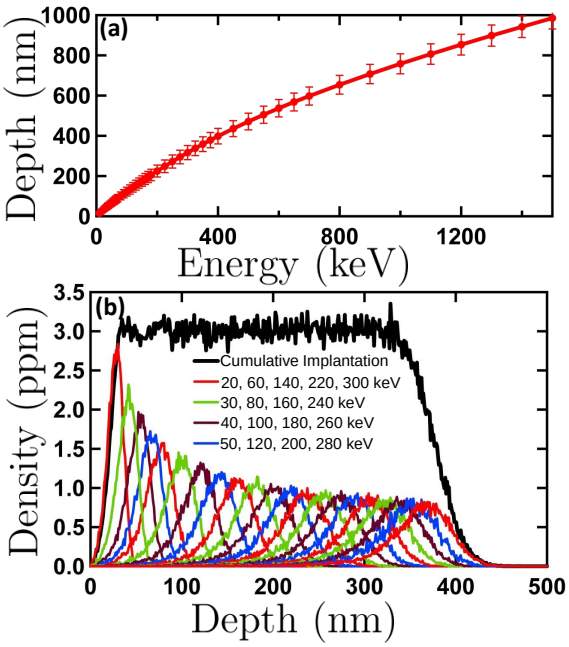

FIG. 13: The results of the theoretical design of a custom ion implanted diamond sample conducted using publicly available SRIM and TRIM software. (a) Depth of nitrogen ion implantation in diamond vs nitrogen ion energy. Error bars represent the expected spread of the implantation depth. (b) Theoretically designed diamond ion implantation density of ∼3 ppm uniform over ∼400 nm ion penetration depth (shown with black line) achieved by combining shown nitrogen ion implantation profiles at multiple implantation energies. This ion implantation scheme was used to fabricate the custom diamond sample used in the research presented in this report.

ppm $= 2 \times 10^{-17}\ cm^{-3}$) of nitrogen P1 centers and about 10^{-5} ppm of N-V centers. The high pressure and high temperature diamond contain significantly more nitrogen impurities. Using the continuous wave EPR we measured the P1 center densities of the HPHT diamond from Element 6 to be about 200 ppm and from Sumitomo to be about 90 ppm. Neither company guarantees the density of P1 centers in delivered HPHT samples. As a result, the density of P1 centers can vary significantly in a commercial HPHT diamond sample thus making such a sample not very useful for the purposes of ESR FMRFM development. In addition, high density of P1 centers results in fast electron spin relaxation thus making such a system a poor choice as a sample for the study of electron spin dynamics.

As a result, diamond samples with the P1 center density in the range of 1-100 ppm cannot be purchased commercially. However, diamond samples with P1 center density of ∼10 ppm would be the optimal choice for the study of electron spin dynamics since they possess still relatively long spin relaxation time but can already exhibit effects of spin-spin interaction. In response to this challenge, we have decided to fabricate custom diamond samples with the well defined P1 center density by custom nitrogen ion implantation of commercial CVD diamond samples.

Ion implantation at a single ion energy results in a nonuniform spatial distribution of the deposited atoms (nitrogen in our case), while we are interested in a uniform spatial distribution of nitrogen atoms in a diamond sample. In this light we have theoretical designed a custom ion implanted diamond sample using publicly available SRIM and TRIM software [27]. Fig. 13 shows the resulting theoretically designed diamond ion implantation density profile of ∼3 ppm uniform over ∼400 nm ion penetration depth (shown with black line) achieved by combining shown nitrogen ion implantation profiles at multiple implantation energies. This ion implantation scheme was used to fabricate the custom diamond sample used in the research presented in this report.

Nitrogen ion implantation was done at the commercial implantation service Leonard Kroko Implantation [28] following the implantation scheme devised using SRIM and TRIM software. During the implantation the sample was at room temperature. After implantation the sample was annealed at 900 C in the forming gas atmosphere (4% H_2 in Ar) in order to repair damage introduced by ion irradiation [29, 30]. Using this approach we have fabricated two types of test samples for ESR MRFM

- Sample with uniform ion implantation profile over the entire sample surface
- Samples with patterned implantation regions

fabricated via ion implantation through a gold mask deposited on sample surface

Uniform samples allow rapid verification of the results of ion implantation since they do not require to search for the ion implantation region once the sample is cooled to liquid He temperature. On the other hand patterned samples present a much more interesting target for ESR MRFM imaging and for the study of dynamic spin effects such as spin diffusion.

The results of the experimental studies of the custom fabricated samples will be presented in a manuscript "The effect of spin transport on lifetime in nanoscale systems" that is currently under review in *Nature Nanotechnology*.

VIII. SIMULTANEOUS MEASUREMENT OF P1 AND NV CENTERS IN DIAMOND

This experiment was using a custom fabricated uniformly implanted diamond sample with the designed P1 center density of 3 ppm. It is known that nitrogen ion implantation followed by annealing results also in creation of N-V centers [31]. Our experimental data shown in Fig. 14 demonstrates simultaneous detection of P1 and N-V centers in diamond. The experimental data (shown with green dots) clearly exhibits a double Lorentzian structure signifying existence of two electron spin populations with different lifetimes. The blue and red curves are the individual Lorentzians fitting the experimental curve. The blue curve has a longer lifetime of 220 ms and corresponds to a fewer spins which is the signature of N-V center population. The red curve, corresponding to a larger spin population, has a shorter lifetime of 12 ms and, undoubtedly, originates from P1 centers. Based on this data, we estimate that the density of the observed N-V centers is $\sim$0.1 ppm which is in a good agreement with the expected N-V center generation rate [31]. This experimental data demonstrates the ability of ESR MRFM to simultaneously detect and distinguish between two electron spin populations with different lifetimes. Such a capability is important for the study of spin systems of practical scientific significance.

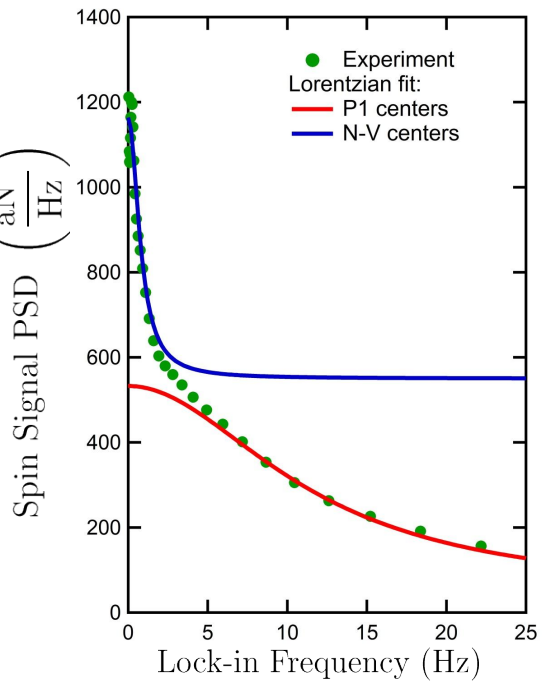

FIG. 14: A force power spectrum density (PSD) on the MRFM cantilever demonstrating simultaneous detection of P1 and N-V centers in diamond. The experimental data (shown with green dots) clearly exhibits a double Lorentzian structure signifying existence of two electron spin populations with different lifetimes. The blue and red curves are the individual Lorentzians fitting the experimental curve. The blue curve has a longer lifetime of 220 ms and corresponds to a fewer spins which is the signature of N-V center population. The red curve corresponding to a larger spin population has a shorter lifetime of 12 ms and, undoubtedly, originates from P1 centers. The blue curve is offset for clarity.

IX. ENDOR AND EPR CHARACTERIZATION OF P_1 CENTERS IN DIAMOND

Electron Nuclear Double Resonance (ENDOR) is a very attractive approach to measuring an individual *nuclear* spin magnetic resonance through detecting the dynamics of an *electron* spin coupled to the nuclear spin through hyperfine cou-

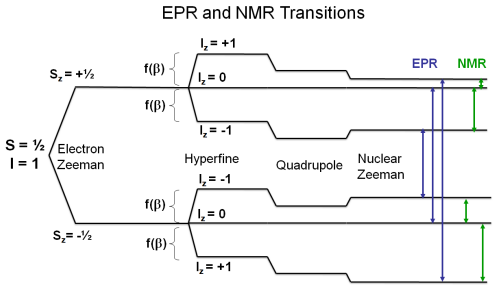

FIG. 15: Energy level diagram of the ^{14}N P_1 center in diamond with the electron spin of 1/2 and the nuclear spin of 1.

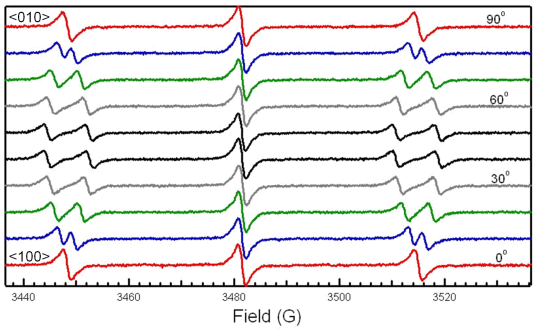

FIG. 16: Conventional CW P_1 center EPR in diamond measured as a function of the sample orientation relative the applied magnetic field measured at temperature $T = 300$ K and microwave frequency $f = 9.4$ GHz. The orientation of the applied magnetic field was varied relative to the $\langle 100 \rangle$ axis of the diamond sample. When magnetic field is aligned along $\langle 100 \rangle$, all four types of P_1 centers form the same angle β with the magnetic field thus resulting three identical EPR lines. As magnetic field is rotated towards the $\langle 010 \rangle$ direction, P_1 centers split in two groups by the magnitude of the resulting angle β which is manifested by splitting $I_z = \pm 1$ EPR transitions into two lines.

pling. In this method, the requirements on the MRFM force detection sensitivity is relaxed due to the fact the electron magnetic moment μ_e is approximately 1000 times greater than that of an individual nuclear spin μ_n. Though this type of nuclear spin detection will be applicable only to systems with strong electron-nuclear hyperfine coupling, demonstration of an individual *nuclear* spin detection using ENDOR will be an important step towards detecting individual *nuclear* spin directly.

We have chosen nitrogen doped diamond as a test system for demonstrating ENDOR nuclear spin detection using MRFM. Diamond is composed of two interpenetrating face centered cubic (FCC) structures of carbon atoms. Doping a diamond crystal with nitrogen results in the formation of so-called P_1 centers in which a nitrogen atom substitutes for carbon. Substitution of Nitrogen with its extra valence electron relative to carbon results in an unpaired electron shared by the nitrogen and one of the four carbon atoms. Hence there are four equivalent P_1 centers aligned along one of four directions: $\langle 111 \rangle$, $\langle \bar{1}11 \rangle$, $\langle 1\bar{1}1 \rangle$, and $\langle 11\bar{1} \rangle$. The resulting energy configuration of the P_1 center will depend on whether the nitrogen atom is ^{14}N with nuclear spin $I = 1$ or ^{15}N with nuclear spin $I = 1/2$. Since ^{14}N has natural abundance of 99.632% the most common electron-nuclear configuration of the P_1 center has $S = 1/2$ and $I = 1$ with the resulting electron-nuclear Hamiltonian $\mathcal{H}$ given by:

$$\frac{\mathcal{H}}{h} = v_e S_z + S_z I_z \sqrt{A_{||}^2 \cos^2\beta + A_{\perp}^2 \sin^2\beta} + P I_z^2 \cos^2\beta - v_n I_z,$$

where v_e is the electron spin resonance frequency, $A_{||}$ and $A_{\perp}$ are the hyperfine coupling parallel and perpendicular to the direction of the carbon-nitrogen bond, P is the nuclear quadrupole coupling, v_n is the nitrogen nuclear magnetic resonance frequency, β is the angle made by the applied magnetic field with the direction of carbon-nitrogen bond, S_z and I_z are the z (parallel to applied magnetic field) components of the electron and nuclear spin. The resulting P_1 energy diagram is shown in Fig.15. These energy characteristics make P_1 centers in diamond an ideal sample for demonstrating ENDOR detection with MRFM.

We have acquired a nitrogen doped diamond

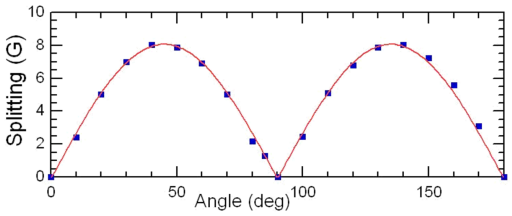

FIG. 17: Observed splitting of $I_z = \pm 1$ peaks as a function of orientation of applied magnetic field. Blue squares represent measured peak splitting and solid line is the fit of the data with Eq. 27 using $A_{||}$ and $A_\perp$ as fitting parameters. The independent variable is the angle made by applied field $\mathbf{H}_0$ with $\langle 100 \rangle$ axis.

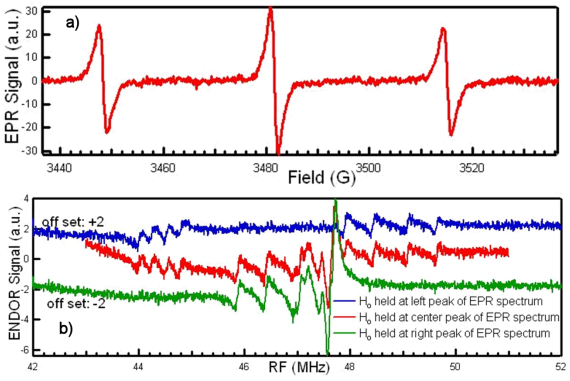

FIG. 18: Conventional EPR and ENDOR spectra of P_1 center in diamond acquired with applied magnetic field H_0 aligned along the $\langle 100 \rangle$ direction of the diamond crystal. a) Conventional P_1 EPR signal demonstrating EPR transitions indicated in Fig. 15 acquired at applied μ-wave frequency $f_{\mu w} = 9.4$ GHz. b) Conventional P_1 ENDOR spectra acquired with external magnetic field H_0, combined with the μ-wave frequency $f_{\mu w} = 9.4$ GHz, set to select one of the EPR transitions with I_z =1, 0 or -1 (as indicated in Fig. 15). ENDOR spectra are shown as a function of frequency of applied rf radiation. ENDOR spectra a offset for clarity. The resulting spectra have all the features expected from the hyperfine coupled electron-nuclear system. As $f_{\mu w}$ is aligned with the side peaks ($I_z = \pm 1$) of the EPR spectrum, we observe signatures of two NMR transitions (as can be seen in Fig. 15). Each transition is split into four individual lines due to slight misalignment of magnetic field with the $\langle 100 \rangle$ direction resulting four slightly different angles with carbon-nitrogen bond. As $f_{\mu w}$ is aligned with the central ($I_z = 0$) EPR peak, we observe four NMR transitions (as can be seen in Fig. 15). Each transition is yet again split into four lines due to field misalignment. In the ENDOR spectrum shown in b) some NMR lines overlap thus somewhat obscuring the observed picture.

sample from a commercial supplier, Element Six (http://www.e6.com). The sample has dimensions 2.7 mm $\times$ 2.7 mm $\times$ 0.5 mm with an expected P_1 center concentration of 200 ppm. Prior to the MRFM experiment it is essential to characterize the sample by conventional EPR/ENDOR means with the main objective to verify a sufficient concentration of P_1 centers and confirm the strength of the hyperfine coupling. These experiments were conducted using Bruker Electron Spin Resonance (ESR) Spectrometer acquired with funds from the ARO DURIP grant W911NF-07-1-0305. The experimental results are presented below.

With availability of four equivalent P_1 centers indicated by three allowed EPR transitions each (See Fig. 15), the resulting EPR spectrum is strongly dependent on the orientation of the applied external magnetic field relative to the axis of the diamond crystal. Depending on the orientation of the field the EPR transitions corresponding to $I_z = \pm 1$ can be split by the hyperfine coupling into up to four EPR lines due to four different angles between the magnetic field and the direction of the carbon-nitrogen bond. This dependence can be exploited to measure the strength of the hyperfine coupling as shown in Fig. 16 showing CW EPR measurements done on P_1 centers diamond at temperature $T = 300$ K and microwave frequency $f = 9.4$ GHz. In the experiment EPR spectra were measured as a function of the sample orientation relative the applied magnetic field. As magnetic field is aligned with the $\langle 100 \rangle$ direction of the crystal, all four types of P_1 centers form the same angle β with the magnetic field thus resulting three identical EPR lines. As magnetic field is rotated towards the $\langle 010 \rangle$ direction, P_1 centers split in two groups

by the magnitude of the resulting angle β which is manifested by splitting $I_z = \pm 1$ EPR transitions into two lines as demonstrated in Fig. 16.

The angular dependence of the $I_z = \pm 1$ line splitting ΔK is described by:

$$\Delta K = \sqrt{A_{||}^2 \cos^2\beta_1 + A_{\perp}^2 \sin^2\beta_1} - \sqrt{A_{||}^2 \cos^2\beta_2 + A_{\perp}^2 \sin^2\beta_2}, \quad (27)$$

where β_1 and β_2 are the angles between the magnetic field and the carbon-nitrogen bond for the two groups of P_1 centers. This equation was used to fit experiments data as shown in Fig. 17 showing observed splitting of $I_z \pm 1$ peaks as a function of orientation of applied magnetic field. Blue squares represent measured peak splitting and solid line is the fit of the data with Eq. 27 using $A_{||}$ and $A_{\perp}$ as fitting parameters. The angle on the x-axis is the angle made by applied field H_0 with $\langle 100 \rangle$ axis.

The values of longitudinal and transverse hyperfine splitting obtained from this data fit are $A_{||} = 40.7 \pm 0.1$ G and $A_{\perp} = 29.3 \pm 0.1$ G. These results are in a good agreement with the values available in literature [32] with $A_{||} = 40.24$ G, $A_{\perp} = 29.73$ G. These results also confirm that the sample has a sufficient P_1 center density and is therefore suitable for ENDOR MRFM experiments.

We have conducted conventional ENDOR experiments using our CW EPR spectrometer; results are shown in Fig. 18. The applied magnetic field H_0 was aligned parallel to $\langle 100 \rangle$ resulting in a simple EPR spectrum with three EPR lines (Fig. 18a). The microwave frequency $f_{\mu w}$ was set to a fixed value matching one of the three EPR transitions. With $f_{\mu w}$ fixed, an ENDOR spectrum was recorded as a function of the frequency $f_{\rm rf}$ of the applied rf radiation generated by an additional rf source. The resulting spectra have all the features expected from the hyperfine coupled electron-nuclear system. As $f_{\mu w}$ is aligned with the side peaks ($I_z = \pm 1$) of the EPR spectrum, we observe signatures of two NMR transitions (see Fig. 15). Each transition is split into four individual lines due to a slight misalignment of the magnetic field with the $\langle 100 \rangle$ direction resulting four slightly different angles with carbon-nitrogen bond. When $f_{\mu w}$ matches the central ($I_z = 0$) EPR peak, we observe four NMR transitions (as can be seen in Fig. 15). Each transition is yet again split into four lines due to field misalignment, hence we see 16 transitions in all. In the ENDOR spectrum shown in Fig. 18b some NMR lines overlap thus somewhat obscuring the picture.

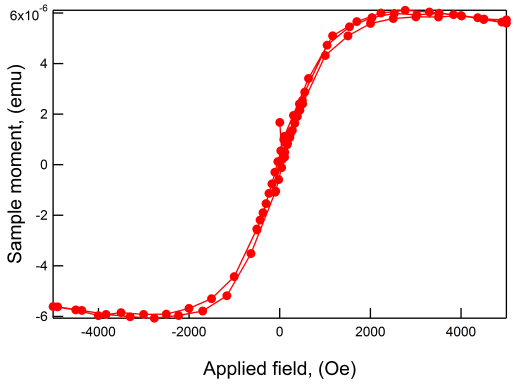

FIG. 19: LAO/STO sample hysteresis curve, shown with diamagnetic background subtracted, measured using a SQUID magnetometer. The data was acquired at 300 K.

In conclusion, we have successfully characterized nitrogen doped diamond sample and have confirmed its suitability for use in ENDOR MRFM experiments.

X. INTERFACE MAGNETISM IN LAO/STO

We have conducted preliminary investigations of physical systems that might serve as samples for future ESR-MRFM studies. The systems of particular interest would exhibit magnetic properties at nanoscale. Such a system would require use of ESR-MRFM for its studies, since the conventional magnetic resonance techniques do not have sensitivity necessary for the study of nanoscale samples, thus highlighting the advantages of the ESR-MRFM over other experimental approaches. One of the promis-

ing systems in this regard is the 2D interface in $LaAlO_3/SrTiO_3$(LAO/STO) system where interesting magnetic properties have been reported including coexistence of ferromagnetism and superconductivity [33]. High spin sensitivity and the high spatial resolution of MRFM will be invaluable for the study of such a system. As it is common with with ESR-MRFM applications, the potential samples have to be characterized by conventional techniques.

We performed a series of SQUID measurements on an LAO/STO sample. The sample was grown by the group of Prof. C. H. Ahn at Yale University (New Haven, CT). The sample has metallic interface states that were confirmed by measuring the conductivity as a function of temperature, finding a sheet resistance of 1000 Ω/square at a temperature of 2 K.

We collected hysteresis curves to investigate the ferromagnetism as reported in the literature [34]. For our measurements, we took both field cooled, and zero-field cooled scans at a variety of temperatures, since the literature reports an increase in magnetic moment at low temperatures with the example of acquired hysteresis curve shown in Fig. 19. Our measurements show a strong diamagnetic background, which we attribute to the bulk STO substrate, but they also reveal weak ferromagnetism that is roughly independent of temperature. This result is surprising given that the moment is expected to grow with decreasing temperature. Upon further investigation, we concluded that this effect must be due to contaminants on the unpolished surfaces of the STO substrate, which has been found to yield weak ferromagnetic signal [35]. We can conclude that that the net magnetic moment at the LAO/STO interface was smaller than 10^{-6} emu, the limit of the SQUID that was used for measurement. Thus, this might mean that ESR-MRFM might be one of the few methods for the study of magnetism at LAO/STO interface.

[1] S.-Y. Lee, M. Widmann, T. Rendler, M. W. Doherty, T. M. Babinec, S. Yang, M. Eyer, P. Siyushev, B. J. M. Hausmann, M. Loncar, Z. Bodrog, A. Gali, N. B. Manson, H. Fedder and J. Wrachtrup. "Readout and control of a single nuclear spin with a metastable electron spin ancilla." *Nat Nano*, **8**(7) 487–492 (2013)

[2] L. Childress, M. V. Gurudev Dutt, J. M. Taylor, A. S. Zibrov, F. Jelezko, J. Wrachtrup, P. R. Hemmer and M. D. Lukin. "Coherent Dynamics of Coupled Electron and Nuclear Spin Qubits in Diamond." *Science*, **314**(5797) 281–285 (2006)

[3] G. Balasubramanian, P. Neumann, D. Twitchen, M. Markham, R. Kolesov, N. Mizuochi, J. Isoya, J. Achard, J. Beck, J. Tissler, V. Jacques, P. R. Hemmer, F. Jelezko and J. Wrachtrup. "Ultralong spin coherence time in isotopically engineered diamond." *Nat Mater*, **8**(5) 383–387 (2009)

[4] T. Kennedy, J. Colton, J. Butler, R. Linares and P. Doering. "Long coherence times at 300 K for nitrogen-vacancy center spins in diamond grown by chemical vapor deposition." *Applied physics letters*, **83**(20) 4190–4192 (2003)

[5] S. Takahashi, R. Hanson, J. van Tol, M. S. Sherwin and D. D. Awschalom. "Quenching Spin Decoherence in Diamond through Spin Bath Polarization." *Phys. Rev. Lett.*, **101** 047601 (2008)

[6] W. Pfaff, T. H. Taminiau, L. Robledo, H. Bernien, M. Markham, D. J. Twitchen and R. Hanson. "Demonstration of entanglement-by-measurement of solid-state qubits." *Nat Phys*, **9**(1) 29–33 (2013)

[7] S. Zhang, B. H. Meier and R. R. Ernst. "Polarization echoes in NMR." *Phys. Rev. Lett.*, **69** 2149–2151 (1992)

[8] X. Lou, C. Adelmann, S. A. Crooker, E. S. Garlid, J. Zhang, K. M. Reddy, S. D. Flexner, C. J. Palmstrøm and P. A. Crowell. "Electrical detection of spin transport in lateral ferromagnet–semiconductor devices." *Nature Physics*, **3**(3) 197–202 (2007)

[9] F. Jelezko, T. Gaebel, I. Popa, A. Gruber and J. Wrachtrup. "Observation of Coherent Oscillations in a Single Electron Spin." *Phys. Rev. Lett.*, **92** 076401 (2004)

[10] R. Hanson and D. D. Awschalom. "Coherent manipulation of single spins in semiconductors." *Nature*, **453**(7198) 1043–1049 (2008)

[11] G. M. Muller, M. Romer, D. Schuh, W. Wegscheider, J. Hubner and M. Oestreich. "Spin Noise Spectroscopy in GaAs (110)

Quantum Wells: Access to Intrinsic Spin Lifetimes and Equilibrium Electron Dynamics." *Phys. Rev. Lett.*, **101** 206601 (2008)

[12] E. Seitaridou, M. M. Inamdar, R. Phillips, K. Ghosh and K. Dill. "Measuring flux distributions for diffusion in the small-numbers limit." *The Journal of Physical Chemistry B*, **111**(9) 2288–2292 (2007)

[13] E. Reynhardt, G. High and J. Van Wyk. "Temperature dependence of spin-spin and spin-lattice relaxation times of paramagnetic nitrogen defects in diamond." *The Journal of chemical physics*, **109** 8471 (1998)

[14] A. Abragam. *The Principles of Nuclear Magnetism*. Clarendon, Oxford (1961)

[15] B. W. Chui, Y. Hishinuma, R. Budakian, H. J. Mamin, T. W. Kenny and D. Rugar. "Mass-loaded cantilevers with suppressed higher-order modes for magnetic resonance force microscopy." In *TRANSDUCERS, Solid-State Sensors, Actuators and Microsystems, 12th International Conference on, 2003*, vol. 2, pp. 1120–1123. IEEE (2003)

[16] H. J. Mamin, R. Budakian, B. W. Chui and D. Rugar. "Detection and Manipulation of Statistical Polarization in Small Spin Ensembles." *Phys. Rev. Lett.*, **91** 207604 (2003)

[17] D. Rugar, R. Budakian, H. J. Mamin and B. W. Chui. "Single spin detection by magnetic resonance force microscopy." *Nature*, **430** 329–332 (2004)

[18] M. Furis, D. Smith, S. Kos, E. Garlid, K. Reddy, C. Palmstrøm, P. Crowell and S. Crooker. "Local Hanle-effect studies of spin drift and diffusion in n: GaAs epilayers and spin-transport devices." *New Journal of Physics*, **9**(9) 347 (2007)

[19] J. Van Wyk, E. Reynhardt, G. High and I. Kiflawi. "The dependences of ESR line widths and spin-spin relaxation times of single nitrogen defects on the concentration of nitrogen defects in diamond." *Journal of Physics D: Applied Physics*, **30**(12) 1790 (1997)

[20] F. Jedema, H. Heersche, A. Filip, J. Baselmans and B. Van Wees. "Electrical detection of spin precession in a metallic mesoscopic spin valve." *Nature*, **416**(6882) 713–716 (2002)

[21] R. Budakian, H. J. Mamin and D. Rugar. "Suppression of Spin Diffusion near a Micron-Size Ferromagnet." *Physical Review Letters*, **92**(3) 037205 (2004)

[22] A. Z. Genack and A. G. Redfield. "Theory of nuclear spin diffusion in a spatially varying magnetic field." *Phys. Rev. B*, **12** 78–87 (1975)

[23] J. Loubser and J. van Wyk. "Electron spin resonance in the study of diamond." *Reports on Progress in Physics*, **41**(8) 1201 (1978)

[24] W. H. Richards. "Bayesian-based iterative method of image restoration." *J. Opt. Soc. Am.*, **62**(1) 55 (1972)

[25] "Element 6, http://www.e6.com/en/, 35 West 45th St., New York, NY 10036."

[26] "Sumitomo Electric Industries, http://www.sumicarbide.com/materialsgroup/, 1900 Polaris Parkway, Suite 450, Columbus, OH 43240."

[27] J. F. Ziegler. "SRIM software package." www.srim.org

[28] "Kroko Implantation, http://krokoimplants.com/, 2822-D Walnut Ave., Tustin, CA 92780."

[29] R. C. Fletcher and W. L. Brown. "Annealing of Bombardment Damage in a Diamond-Type Lattice: Theoretical." *Phys. Rev.*, **92**(3) 585–590 (1953)

[30] L. Allers, A. T. Collins and J. Hiscock. "The annealing of interstitial-related optical centres in type II natural and CVD diamond." *Diamond and Related Materials*, **7**(2-5) 228 – 232 (1998)

[31] S. Pezzagna, B. Naydenov, F. Jelezko, J. Wrachtrup and J. Meijer. "Creation efficiency of nitrogen-vacancy centres in diamond." *New Journal of Physics*, **12**(6) 065017 (2010)

[32] C. Kedkaew and P. Limsuwan. "The Spin Hamiltonian Parameters Calculation Of 14N And 15N In Natural Type I Diamond." *International Journal of Modern Physics B*, **22** 4740–4748 (2008)

[33] D. A. Dikin, M. Mehta, C. W. Bark, C. M. Folkman, C. B. Eom and V. Chandrasekhar. "Coexistence of Superconductivity and Ferromagnetism in Two Dimensions." *Phys. Rev. Lett.*, **107** 056802 (2011)

[34] J. A. Bert, B. Kalisky, C. Bell, M. Kim, Y. Hikita, H. Y. Hwang and K. A. Moler. "Direct imaging of the coexistence of ferromagnetism and superconductivity at the LaAlO3/SrTiO3 interface." *Nature Physics*, **7**(10) 767–771 (2011)

[35] S. M. M. Yee, D. A. Crandles and L. V. Goncharova. "Ferromagnetism on the unpolished surfaces of single crystal metal oxide substrates." *J. App. Phys.*, **110**(3) (2011)